

Chapter 1

Broadband Electrical Impedance Tomography for Subsurface Characterization Using Improved Corrections of Electromagnetic Coupling and Spectral Regularization

Andreas Kemna, Johan A. Huisman, Egon Zimmermann, Roland Martin, Yulong Zhao, Andrea Treichel, Adrian Flores Orozco and Thomas Fechner

Abstract The low-frequency complex electrical conductivity in the mHz to kHz range has been shown to enable an improved textural, hydraulic, and biogeochemical characterization of the subsurface using electrical impedance spectroscopy (EIS) methods. Principally, these results can be transferred to the field using electrical impedance tomography (EIT). However, the required accuracy of 1 mrad in the phase measurements is difficult to achieve for a broad frequency bandwidth because of electromagnetic (EM) coupling effects at high frequencies and the lack of inversion schemes that consider the spectral nature of the complex electrical conductivity. Here, we overcome these deficiencies by (i) extending the standard spatial-smoothness constraint in EIT to the frequency dimension, thus enforcing smooth spectral signatures, and (ii) implementing an advanced EM coupling removal procedure using a newly formulated forward electrical model and calibration measurements. Both methodological advances are independently validated, and the improved imaging capability of the overall methodology with respect to spectral electrical properties is demonstrated using borehole EIT measurements in a heterogeneous aquifer. The developed procedures represent a significant step forward towards broadband EIT, allowing transferring the considerable diagnostic potential of EIS in the mHz to kHz

A. Kemna (✉) · R. Martin · A. Flores Orozco
Geodynamics/Geophysics, Steinmann Institute, University of Bonn, Meckenheimer
Allee 176, 53115 Bonn, Germany
e-mail: kemna@geo.uni-bonn.de

J. A. Huisman · A. Treichel
Forschungszentrum Jülich GmbH, Institute for Bio- and Geosciences – Agrosphere (IBG 3),
52425 Jülich, Germany

E. Zimmermann · Y. Zhao
Forschungszentrum Jülich GmbH, Central Institute for Engineering, Electronics, and Analytics –
Electronic systems (ZEA 2), 52425 Jülich, Germany

T. Fechner
Geotomographie GmbH, Am Tonnenberg 18, 56567 Neuwied, Germany

range to geophysical imaging applications at the field scale for improved subsurface characterization.

1.1 Introduction

Spectral induced polarization (SIP), also known as electrical impedance spectroscopy (EIS), is a geophysical method to measure the frequency-dependent complex electrical conductivity of soils, sediments, and rocks in the mHz to kHz range. In the absence of electronically conducting minerals, the real part of the complex electrical conductivity is a measure of ionic conduction in the water-filled pores and along water-mineral interfaces. The imaginary part of the complex conductivity is a measure of ionic polarization in response to an external electric field associated with electrically charged mineral surfaces and constrictions in the pore space (e.g., Leroy et al. 2008; Revil 2013). EIS can be implemented in a tomographic framework (e.g., Kemna et al. 2000), and is then commonly referred to as electrical impedance tomography (EIT).

In the last decades, EIS and EIT have been increasingly used in a wide range of applications, including lithological and textural characterization (e.g., Vanhala 1997; Slater and Lesmes 2002), direct estimation of hydraulic conductivity (e.g., Kemna et al. 2004; Binley et al. 2005; Revil and Florsch 2010), delineation of contaminant plumes (e.g., Kemna et al. 2004; Flores Orozco et al. 2012a), and monitoring of biogeochemical processes associated with contaminant remediation (e.g., Williams et al. 2009; Flores Orozco et al. 2013). The potential of EIS measurements for these applications has been clearly demonstrated in laboratory studies. It arises from the fact that the complex conductivity is directly affected by pore space geometry, pore fluid chemistry, and mineral surface properties. However, it is currently still difficult to fully capitalize on the recognized diagnostic capabilities of EIS measurements in EIT field applications (Kemna et al. 2012).

A first difficulty that currently limits the value of EIT measurements is that existing EIT inversion approaches treat all frequencies independently. This may lead to inconsistent imaging results that do not adequately capture the smooth and relatively weak frequency dependence of the complex electrical conductivity that has been reported in most studies dealing with the electrical properties of soils, sediments, and rocks.

A second reason why currently EIT is not able to deliver its full potential is related to the required high accuracy of 1 mrad in the phase measurements over a broad frequency range, extending from mHz to kHz. In recent years, considerable progress has been made with respect to understanding, quantifying, and correcting different error sources present in laboratory EIS and EIT measurements above 10 Hz (Zimmermann et al. 2008a, b). Despite this instrumental progress, it is still not possible to achieve such a high accuracy for a broad frequency bandwidth in EIT field applications. This is related to electromagnetic (EM) coupling effects that considerably affect EIT measurements at frequencies above ~ 10 Hz (e.g., Madden

and Cantwell 1967). This EM coupling is mainly caused by capacitive and inductive coupling between the electrical wires or between the wires and the soil and is thus inherent to field EIT measurements.

Within this context, the project ‘4D Spectral Electrical Impedance Tomography—a diagnostic imaging tool for the characterization of subsurface structures and processes (4DEIT)’ was formulated. The main aims of this project were threefold. A first aim was to extend the standard spatial-smoothness constraint in EIT to the frequency dimension in order to obtain consistent imaging results across multiple frequencies. The developed approach was implemented in an existing EIT inversion code and validated using laboratory EIT measurements. A second aim was to develop correction procedures for inductive and capacitive coupling in EIT measurements made with multi-electrode chains. Controlled test measurements in a water-filled container were used for initial validation of the correction procedures and to determine the maximum expected accuracy that can be achieved using EIT field measurements of the complex electrical conductivity. A final aim was to evaluate these methodological advances using borehole EIT measurements made in the heterogeneous aquifer of the Krauthausen test site. In the following, we report on the main scientific findings of the 4DEIT project.

1.2 Inversion Methodology

1.2.1 EIT Inversion Approach

Electrical impedance tomography involves the inversion of a set of transfer impedances, Z , measured on an array of electrodes using a series of individual four-electrode configurations, into a distribution of complex resistivity, $\rho = |\rho| e^{j\phi}$ (with resistivity magnitude $|\rho|$, resistivity phase ϕ , and imaginary unit $j^2 = -1$), or complex electrical conductivity $\sigma = |\sigma| e^{-j\phi} = \sigma' + i\sigma''$ (with conductivity magnitude $|\sigma| = 1/|\rho|$, conductivity phase $-\phi$, real part of conductivity σ' , and imaginary part of conductivity σ'').

We here build upon the finite-element based, smoothness-constraint inversion code by Kemna (2000), in which log-transformed impedances are used as data and log-transformed complex conductivities (of lumped finite-element cells) as parameters to account for the large range of resistance values in typical EIT data sets and of resistivity values for earth materials, respectively. For standard single-frequency, i.e., non-spectral, applications, the algorithm follows a standard Gauss-Newton procedure for non-linear inverse problems and iteratively minimizes an objective function, $\Psi(\mathbf{m})$, composed of the measures of data misfit and spatial model roughness, with both terms being balanced by a regularization parameter λ :

$$\Psi(\mathbf{m}) = \|\mathbf{W}[\mathbf{d} - \mathbf{f}(\mathbf{m})]\|^2 + \lambda \|\mathbf{R}\mathbf{m}\|^2, \quad (1.1)$$

where \mathbf{d} is the data vector, \mathbf{m} the model vector, $\mathbf{f}(\mathbf{m})$ the operator of the finite-element forward model, \mathbf{W} a data weighting matrix, and \mathbf{R} a (real-valued) matrix evaluating the (first-order) spatial roughness of \mathbf{m} . Under the assumption that the data errors are uncorrelated and normally distributed, \mathbf{W} is a diagonal matrix, with its entries in this study being estimated from the analysis of impedance data pairs measured in normal and reciprocal configurations (Koestel et al. 2008; Flores Orozco et al. 2012b). At each iteration step, a univariate search is performed to find the optimum value of the regularization parameter λ which locally minimizes the data misfit. The model update, $\Delta\mathbf{m}$, is calculated from solving the linear system of equations

$$\left[\mathbf{J}^H \mathbf{W}^H \mathbf{W} \mathbf{J} + \lambda \mathbf{R}^T \mathbf{R} \right] \Delta\mathbf{m} = \mathbf{J}^H \mathbf{W}^H \mathbf{W} [\mathbf{d} - \mathbf{f}(\mathbf{m})] - \lambda \mathbf{R}^T \mathbf{R} \mathbf{m}, \quad (1.2)$$

where \mathbf{J} is the Jacobian matrix computed for the given model \mathbf{m} , H denotes the Hermitian (complex conjugate transpose), and T the transpose matrix. The iteration process is stopped when the root-mean-square data-misfit value reaches the value of 1 for a maximum possible λ , yielding the smoothest spatial distribution explaining the data.

1.2.2 EIT Inversion with Spatio-Spectral Regularization

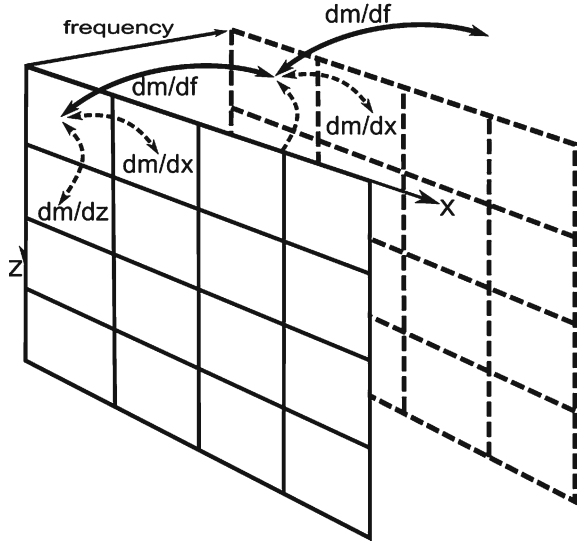
Current complex conductivity (or complex resistivity) imaging approaches are limited to the inversion of single-frequency data (e.g., Kemna et al. 2004; Blaschek et al. 2008), or the independent inversion of multi-frequency data sets (e.g., Kemna et al. 2000; Flores Orozco et al. 2012a, 2013). Such an approach limits the characterization capabilities of EIT because there is no control on the spectral behavior in the inversion procedure, resulting in considerable ill-posedness with respect to the retrieval of spectral characteristics. In order to overcome this deficiency, we implemented an extended EIT inversion scheme with full spatio-spectral regularization for the simultaneous inversion of multi-frequency impedance data sets by adding an additional smoothness constraint with respect to the spectral dimension.

Let \mathbf{m}_f , \mathbf{d}_f , \mathbf{J}_f , and \mathbf{W}_f denote the extended model vector, the data vector, the Jacobian matrix, and the data weighting matrix, respectively, that contain all model vectors \mathbf{m}_i , data vectors \mathbf{d}_i , Jacobian matrices \mathbf{J}_i , and data weighting matrices \mathbf{W}_i for N measurement frequencies ($i = 1, \dots, N$):

$$\mathbf{m}_f = \begin{pmatrix} \mathbf{m}_1 \\ \vdots \\ \mathbf{m}_N \end{pmatrix}, \mathbf{d}_f = \begin{pmatrix} \mathbf{d}_1 \\ \vdots \\ \mathbf{d}_N \end{pmatrix}, \mathbf{J}_f = \begin{pmatrix} \mathbf{J}_1 & & \\ & \ddots & \\ & & \mathbf{J}_N \end{pmatrix}, \mathbf{W}_f = \begin{pmatrix} \mathbf{W}_1 & & \\ & \ddots & \\ & & \mathbf{W}_N \end{pmatrix}. \quad (1.3)$$

Note that \mathbf{J}_f and \mathbf{W}_f are block diagonal matrices. For simultaneously inverting the data \mathbf{d}_f we solve the extended linear system of equations

Fig. 1.1 Spatio-spectral regularization scheme implemented in the multi-frequency EIT inversion. The indicated planes represent the spatial model parameterization (lumped finite-element cells in the x,z -plane) at two successive frequencies (f). In addition to its adjacent neighbors in space, each model parameter is coupled to its adjacent “spectral” neighbor (same location in space, but for next frequency)



$$\left[\mathbf{J}_f^H \mathbf{W}_f^H \mathbf{W}_f \mathbf{J}_f + \lambda \mathbf{R}_f^T \mathbf{R}_f \right] \Delta \mathbf{m}_f = \mathbf{J}_f^H \mathbf{W}_f^H \mathbf{W}_f [\mathbf{d}_f - \mathbf{f}_f(\mathbf{m}_f)] - \lambda \mathbf{R}_f^T \mathbf{R}_f \mathbf{m}_f, \quad (1.4)$$

with correspondingly extended forward model response \mathbf{f}_f and model update $\Delta \mathbf{m}_f$, where spatio-spectral smoothing is realized by an extended model roughness matrix, \mathbf{R}_f , given by

$$\mathbf{R}_f = \begin{pmatrix} \mathbf{R}_1 & 0 & \dots & 0 \\ 0 & \mathbf{R}_2 & \ddots & \vdots \\ \vdots & \ddots & \ddots & 0 \\ 0 & \dots & 0 & \mathbf{R}_N \end{pmatrix} + \lambda_f \begin{pmatrix} -1 & 0 & \dots & 0 & 1 & 0 & \dots & 0 \\ 0 & \ddots & \ddots & \vdots & \ddots & \ddots & \ddots & \vdots \\ \vdots & \ddots & -1 & 0 & \dots & 0 & 1 & 0 \\ 0 & \dots & 0 & -1 & \ddots & \vdots & \ddots & 1 \end{pmatrix}. \quad (1.5)$$

In Eq.(1.5), \mathbf{R}_i denote the spatial roughness matrices (generally identical for all measurement frequencies), and the second matrix on the right-hand side contains non-zero entries only at the diagonal element and at one off-diagonal element that correspond to the model parameters at the same location in space but for two successive frequencies (Fig. 1.1). Here, the values -1 and 1 are only indicative; actually the true spectral gradient of the model with respect to log frequency is implemented. The spectral regularization strength in the inversion can be adjusted with the additional regularization parameter λ_f .

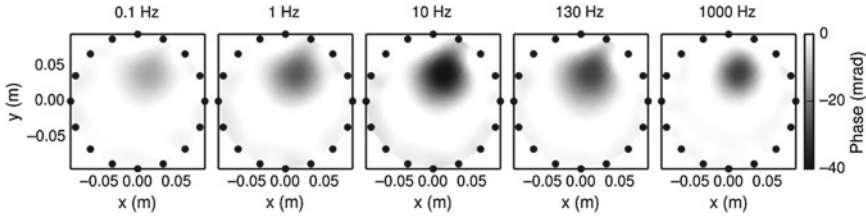


Fig. 1.2 EIT phase images of a cylindrical copper target in a water-filled cylindrical tank at five selected measurement frequencies computed with spatio-spectral regularization. *Black dots* indicate position of electrodes used for data acquisition

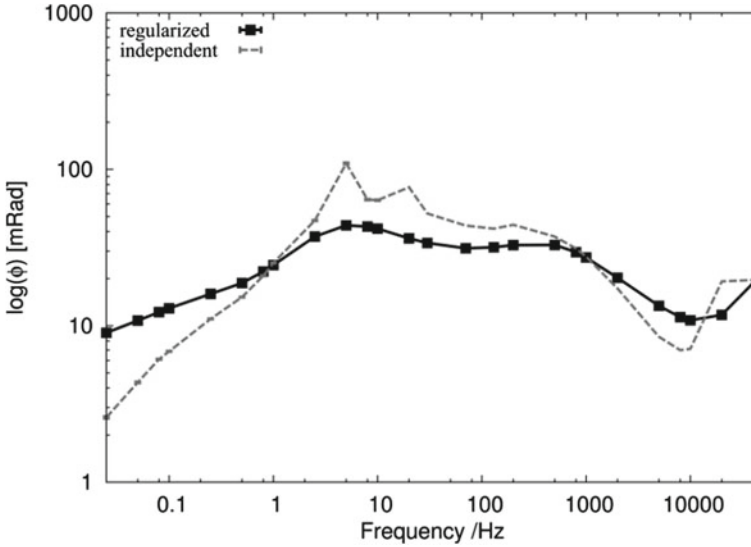


Fig. 1.3 Recovered phase spectrum at the center of the copper target (cf. Fig. 1.2) using independent single-frequency inversions (*dashed grey curve*) and the new multi-frequency inversion with spectral regularization (*solid black curve*)

1.2.3 Validation Using a Physical Tank Model

In order to compare single-frequency inversions with inversion results obtained with additional spectral regularization, EIT measurements were made on a copper cylinder positioned within a water-filled cylindrical tank using the laboratory EIT system described in Zimmermann et al. (2008b). The copper target can easily be identified by the high phase values in the reconstructed images (Fig. 1.2). The phase spectrum extracted from the EIT images at the center of the copper target reveals rather erratic spectral variations, especially in the frequency range between 1 and 100 Hz, where highest polarization is observed for the single-frequency inversions (Fig. 1.3). This reflects the inherent ill-posedness of a non-spectrally regularized inversion approach

with respect to the recovery of spectral variations. With the new spatio-spectral regularization approach, the inverted spectral phase values show a more consistent, smoothly varying behavior, in agreement with the typical dispersion characteristics of electrical relaxation processes. It is clear that the choice of the regularization parameter λ_f in Eq. 1.5 controls the amount of spectral smoothing, and future studies will need to establish methods to determine the most appropriate values of λ_f .

1.3 Inductive and Capacitive Coupling Effects: Modeling and EIT Data Correction

1.3.1 Design of EIT Field System and Borehole Electrode Chains

In order to image the spectral phase response of low-polarizable soils and rocks, spectral EIT measurements with high phase accuracy in a broad frequency range are needed. It is challenging to design EIT data acquisition to achieve such a high accuracy, especially in the high frequency range (100 Hz to 45 kHz). Previous work focused on the development of a laboratory spectral-EIT measurement system with sufficient accuracy (Zimmermann et al. 2008b). On the basis of this laboratory system, a prototype for spectral EIT data acquisition at the field scale was realized (Zimmermann et al. 2010; Zimmermann 2011). Both systems have a modular design with active electrode modules consisting of integrated amplifiers for electric potential measurements and integrated switches for current injection. To achieve the required high accuracy, the developed EIT systems rely on model-based correction methods to minimize the remaining errors of the system. The errors that have been corrected in such a manner are related to amplification, signal drift, and propagation delay of the signal due to the long cables, amongst other error sources.

For borehole EIT measurements, electrode chains and logging tools have recently been developed and constructed. The borehole chains consist of eight active electrode modules with an electrode spacing of 100 cm, whereas the borehole logging tool consists of four electrode modules with an electrode spacing of 16.2 cm. For the electrical connection of the active electrode modules to the EIT data acquisition system, a 25 m long shielded multicore cable is used in both cases (Zhao et al. 2013).

1.3.2 Electromagnetic Coupling

The necessary use of long cables in the design of borehole electrode chains introduces additional errors in the phase measurements due to electromagnetic coupling effects; these effects can be separated in (i) inductive coupling between the long electric loops for current injection and potential measurement, and (ii) capacitive coupling between the cable and the electrically conductive environment. Both types

of coupling currently limit the upper frequency for accurate EIT measurements to the tens of Hz range. The phase errors due to electromagnetically induced eddy currents in the subsurface are small in relation to these two effects and can be neglected for the application considered here.

The inductive coupling using two borehole chains can be divided into two cases: (i) coupling within one electrode chain and (ii) coupling between two different electrode chains. In the first case, the electrical wires in a single multicore cable are close together and this leads to strong inductive coupling. It is important to note that the strength of this coupling depends only on the design of the multicore cable and not on the cable layout during field measurements. In the second case, the coupling is weaker due to the larger separation between the electrical wires. However, the strength of the coupling depends on the position of the multicore cable layout during field measurements, which must therefore be determined or controlled in order to allow adequate corrections for inductive coupling. However, the cable separations only need to be known with cm accuracy. In summary, a configuration with current injection and voltage measurement in one borehole belongs to the first case, and a configuration with current injection in one borehole and voltage measurement in a second borehole belongs to the second case. All other configurations can be obtained by superpositioning of these two types.

Here, we present correction methods for inductive coupling in one multicore cable and capacitive coupling between the borehole chains and the subsurface. The correction of inductive coupling in one cable is a complicated task because the separation between the wires needs to be known with an accuracy better than 0.1 mm. In addition, the inductive coupling is also influenced by eddy currents in the outer shielding of the chain.

1.3.3 Correction Methodology

Inductive coupling leads to a parasitic additive imaginary part in the measured transfer impedances. Typically, a wide range of four-electrode configurations is used to measure the electrical impedance of the subsurface. This electrical transfer impedance Z_M is the ratio of the measured voltage U_M between two potential electrodes and the injected current I_I between two excitation electrodes. Each electrode is connected with one wire which is parallel to the other wires in the case of current injection and voltage measurement in one borehole (Fig. 1.4). The active elements in the electrode modules can be neglected for the consideration of the inductive effects.

Due to the inductive coupling between the two wire pairs, an additional voltage U_{II} in loop II is induced from the injected current I_I in loop I (Fig. 1.4). This means that the injected current leads to an impedance Z_S of the subsurface and the unwanted induced impedance Z_{IC} . This results in the total measured transfer impedance

$$Z_M = Z_S + Z_{IC} = Z_S + j\omega M. \quad (1.6)$$

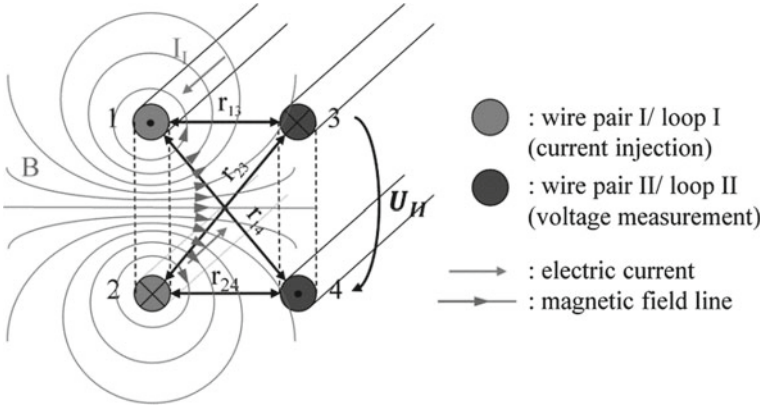


Fig. 1.4 Mutual induction between two parallel electrical wire pairs (from Zhao et al. 2013)

This equation shows that the error due to inductive coupling can be removed by subtracting the coupling impedance Z_{IC} , which is the mutual inductance M multiplied by the imaginary unit j and the angular frequency ω , from the measured transfer impedance.

In order to determine the exact coupling impedances, we have evaluated several approaches. In a first approach, we tried to determine the values based on the geometry of the multicore cable. However, it is not possible to determine the wire positions within the multicore cable with the required accuracy. In addition, eddy currents in the electrical shield have a big influence on the impedance in the kHz frequency range. Therefore, this approach was abandoned. In an alternative approach, we measured the mutual inductance for all possible electrode configurations (Zhao et al. 2013). This is cumbersome and time-consuming for practical use. To overcome this practical problem, the latest calibration method relies on a pole-pole matrix

$$\mathbf{P} = \begin{bmatrix} \mathbf{A} & \mathbf{B} \\ \mathbf{C} & \mathbf{D} \end{bmatrix}, \quad (1.7)$$

with coupling impedances derived from pole-pole calibration measurements. The matrix \mathbf{A} contains the coupling impedances between the wires of the first borehole chain, and the matrix \mathbf{D} contains the coupling impedances between the wires of the second borehole chain. The matrices \mathbf{B} and \mathbf{C} contain the coupling impedances between the wires of different borehole chains. The strength of these couplings depends on the position of the multicore cable layout during field measurements and can be calculated using equations provided in Sunde (1968). This calculation is not treated here. In the future, we will also consider this case of coupling.

In order to obtain the coupling impedances in one borehole chain (matrices \mathbf{A} and \mathbf{D}) using pole-pole (i.e., ground-based) current injection and voltage measurements, all electrodes of the chain are short-circuited and connected to the ground of the

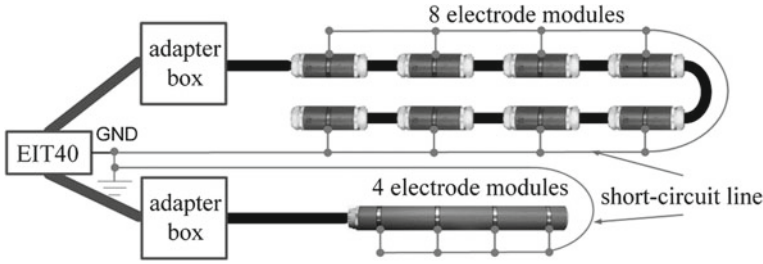


Fig. 1.5 Pole-pole measurement for electrode chain with eight ring electrodes and 25 m long multicore cable, and the logging tool with four electrodes

EIT system (Fig. 1.5). Then, the current is injected at one electrode and the induced voltages are measured at all other electrodes. This measurement is repeated for all electrodes of the chain.

The coupling impedances $Z_{m,n}$ of the pole-pole matrices **A** and **D** are the quotients of the measured induced voltages U_n and the injected currents I_m . In the case of chains with eight electrodes, there are 56 (8×7) measured impedances. The diagonal elements are zero. This yields 8×8 -matrices for **A** and **D**. With the full matrix **P**, the coupling impedance between two arbitrary wire pairs can be calculated using

$$Z_{ABMN} = (Z_{BN} - Z_{AN}) - (Z_{BM} - Z_{AM}), \quad (1.8)$$

where A and B are the numbers of current electrodes and M and N are the numbers of potential electrodes.

Using this approach, we are able to correct impedance measurements for any electrode configuration in a single borehole and later for all configurations. Instead of 840 measurements for all possible configurations in one chain with eight electrodes, only 56 measurements are necessary using this newly developed pole-pole calibration. There are additional additive impedances from the short-circuit wire (Fig. 1.5) that need to be corrected with additional measurements. This issue has not been resolved yet, and needs additional attention.

The parasitic current due to the potential differences between the subsurface and the outer shield of the multicore cable (i.e., capacitive coupling) is the second source of phase errors. The outer shield of the multicore cable is used to shield the inner wires from the environment and is therefore connected with system ground (zero potential). The potential distribution in the subsurface is the wanted result of the current injection. These potential differences to the shield cause uncontrolled parasitic currents across the insulator of the multicore cable. An a-priori calculation of the parasitic currents is not possible, because the potential distribution in the subsurface depends on the unknown electrical conductivity distribution.

In order to consider these capacitive coupling effects, the admittances of discrete capacitances of cable segments are integrated in the finite-element based electrical forward model. The developed method results in a linear system of equations

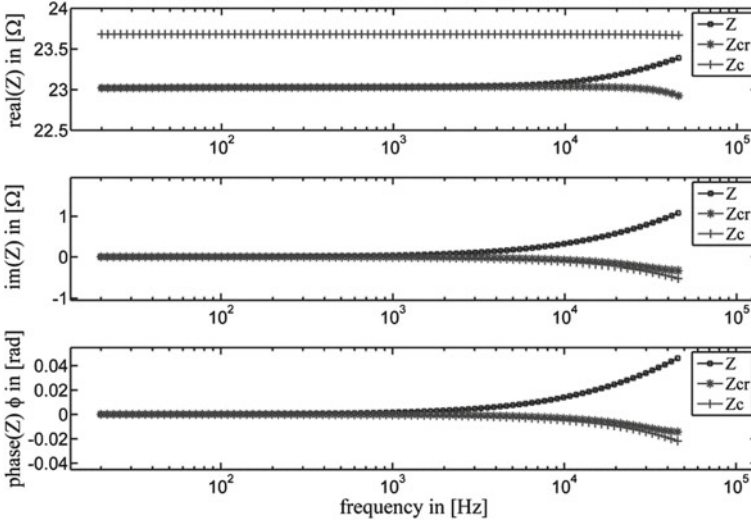


Fig. 1.6 Spectrum of original measured transfer impedances Z , inductive coupling-corrected data Z_{cr} , and modeled data Z_c

$$[\mathbf{Y}_S + \mathbf{Y}_C] \mathbf{U} = \mathbf{I}, \quad (1.9)$$

where \mathbf{U} is the potential and \mathbf{I} the injected current at the nodes of the finite-element modeling mesh. The electrical conductivity distribution in the subsurface is considered within the admittance matrix \mathbf{Y}_S and the admittances of the cable segments are considered with the new matrix \mathbf{Y}_C . The capacities for each node where a capacitance is integrated are calculated on the basis of the outer diameter, the length of the cable segment and the thickness and the permittivity of the insulator. For more details about this modeling we refer to Zimmermann (2011) and Zhao et al. (2013).

1.3.4 Validation of Correction Procedures

The correction methods for inductive and capacitive coupling were verified with a borehole logging tool placed vertically in the center of a water-filled container. The modeled transfer impedance Z_c for a current injection at the outer two electrodes and a voltage measurement between the inner two electrodes of the logging tool can be compared with the measured impedance Z and the impedance Z_{cr} after correction of the inductive coupling (Fig. 1.6). The impedance spectra show an excellent agreement for the imaginary part and the phase angle of the modeled transfer impedances Z_c and the corrected impedance Z_{cr} . The small deviation in the real part is related to geometry errors in the finite-element modeling (e.g., inaccurate electrode positions).

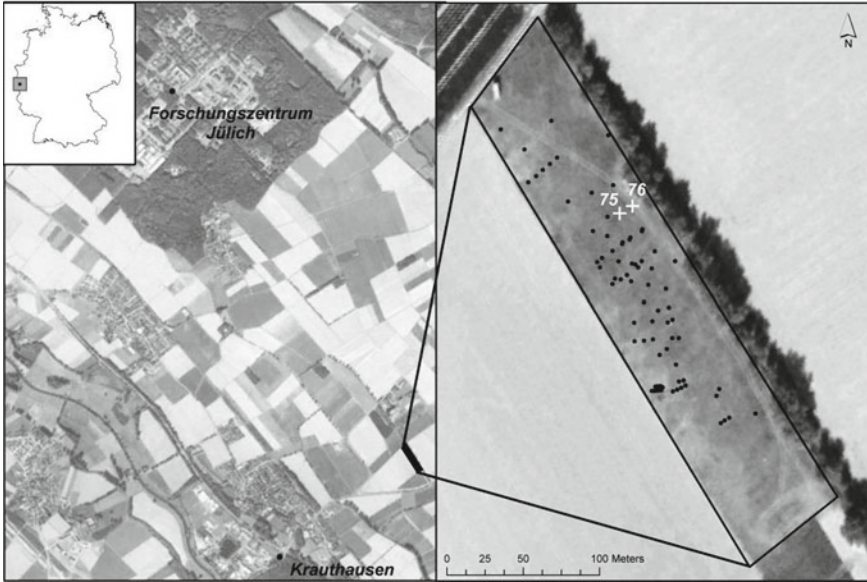


Fig. 1.7 Location of the Krauthausen test site close to the Forschungszentrum Jülich in the Western part of Germany (*left*) and position of monitoring wells, including boreholes 75 and 76, at the site (*right*)

This result shows that a phase accuracy of 1 mrad at 10kHz can be achieved under controlled conditions after accounting for inductive and capacitive coupling effects.

1.4 Field Validation

1.4.1 Krauthausen Test Site

The developed inversion procedure and the correction procedures for inductive and capacitive coupling effects were evaluated by means of borehole EIT measurements at the Krauthausen test site. This test site is situated approximately 10 km northwest of the city of Düren and 6 km southeast of the Forschungszentrum Jülich GmbH, Germany (Fig. 1.7). The upper aquifer is composed of sandy Quaternary deposits with variable gravel content. On top of this aquifer, there is a silty soil layer, and the base of the aquifer consists of silt and clay layers at a variable depth ranging from 11 to 13 m below the surface. The site is equipped with 76, 10–11 m deep observation wells that are screened from 3 m depth downwards (Fig. 1.7).

The hydrogeological characteristics of this test site have been investigated in great detail. Döring (1997) estimated that the geometric mean and variance of the

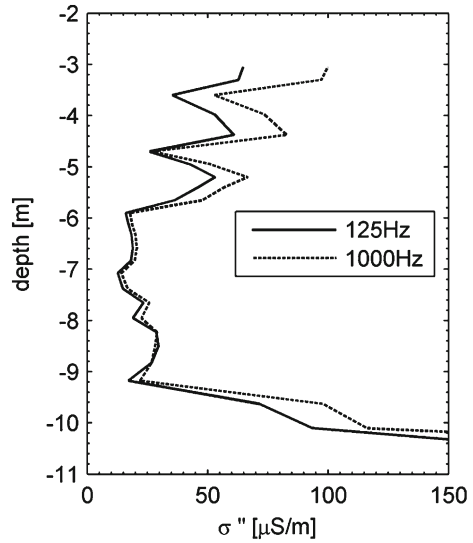
hydraulic conductivity of the aquifer were 0.0013 ms^{-1} and 1.3 (variance of log transformed hydraulic conductivity), respectively. The spatial correlation lengths in the horizontal and vertical directions were determined to be 6.7 m and 0.37 m using cone-penetration tests (Tillmann et al. 2008). The mean porosity is 26 % with a standard deviation of 6 % (Vereecken et al. 2000). The Krauthausen test site has also been the focus of several studies dealing with the application of electrical resistivity tomography to derive hydrologically relevant aquifer properties (e.g., Kemna et al. 2002; Vanderborght et al. 2005; Müller et al. 2010).

1.4.2 Reference EIS Measurements

During drilling and installation of borehole 76 in 2006, aquifer material was collected and visually separated according to layering. This resulted in 29 samples of sediment from a depth range between 1.90 and 10.55 m. After sample collection, the sediment was air-dried and stored for further analysis. The complex electrical conductivity of these samples was determined using an impedance spectrometer that allows accurate EIS measurements for a broad frequency range from 1 mHz to 1 kHz (Zimmermann et al. 2008a). For this, we used a sample holder with a height of 36 cm and a diameter of 6 cm. Two sintered bronze plates were used as current electrodes at the top and bottom of the sample holder, and two ceramic electrodes following the design of Breede et al. (2011) were used as potential electrodes. Before the samples were packed, gravel larger than 1 cm in diameter was removed by sieving. We used the wet-packing method described in Breede et al. (2011) using a CaCl_2 solution with an electrical conductivity of about 0.08 S m^{-1} , which corresponds with the electrical conductivity of the groundwater at the site.

Values of σ'' determined using EIS measurements on repacked samples are provided for two frequencies as a function of depth in Fig. 1.8. According to these measurements, roughly three different layers can be recognized. In the top of the aquifer from 3 to 5 m below surface, σ'' is relatively high and somewhat dependent on frequency. The stronger polarization at 1 kHz as compared to 125 Hz is an indication that the higher σ'' is related to relatively high clay contents in this part of the aquifer. At a depth of 6–7 m below surface, there is a layer with low σ'' values, and in the lowest part of the aquifer, σ'' starts to increase again. There are several issues that complicate a direct transfer of these laboratory EIS measurements to the field, such as the increase in σ' because of the drying and repacking of the laboratory samples and the removal of the gravel fraction before EIS measurements. Nevertheless, we expect that the general pattern and the approximate range of σ'' values should be accurately reproduced by the EIT field measurements.

Fig. 1.8 Imaginary part of the electrical conductivity at 125 Hz (*solid curve*) and 1 kHz (*dashed curve*) as a function of depth obtained from laboratory EIS measurements on repacked Krauthausen sediment samples (without gravel fraction) from borehole 76



1.4.3 EIT Data Acquisition

EIT measurements were made between boreholes 75 and 76 at the Krauthausen test site using borehole electrode chains as described above in each borehole. The groundwater table was located 2.5 m below the surface at the time of the measurements. The uppermost electrode of both electrode chains was placed at a depth of 2.7 m. There were eight electrodes with a separation of 1 m, which means that the deepest electrode of both chains was placed at 9.7 m depth. For current injection, we used all possible electrode configurations for “skip-0” (1–2, 2–3, ..., 9–10, etc.), “skip-2” (1–4, 2–5, etc.), “skip-4” (1–6, 2–7, 3–8), and some configurations for “skip-5” (1–7, 2–8) and “skip-6” (1–8). For the voltage measurements, we used the same electrode pairs except those including current electrodes (e.g., 1–2 4–7, 2–3 1–4, 1–7 2–3), and the corresponding reciprocal measurements (e.g., 4–7 1–2, 1–4 2–3, 2–3 1–7). Prior to the inversion, we corrected the inductive coupling effects by determining $j\omega M$ (Eq. 1.6) for all electrode configurations within a single borehole with the calibration method outlined above. Cross-hole electrode configurations that were known to be hardly affected by inductive coupling were also considered. The remaining cross-hole electrode configurations were not yet considered.

1.4.4 EIT Imaging Results

The EIT field measurements were inverted using two approaches. Initially, only measurements in borehole 76 were considered in an inversion assuming a horizontally

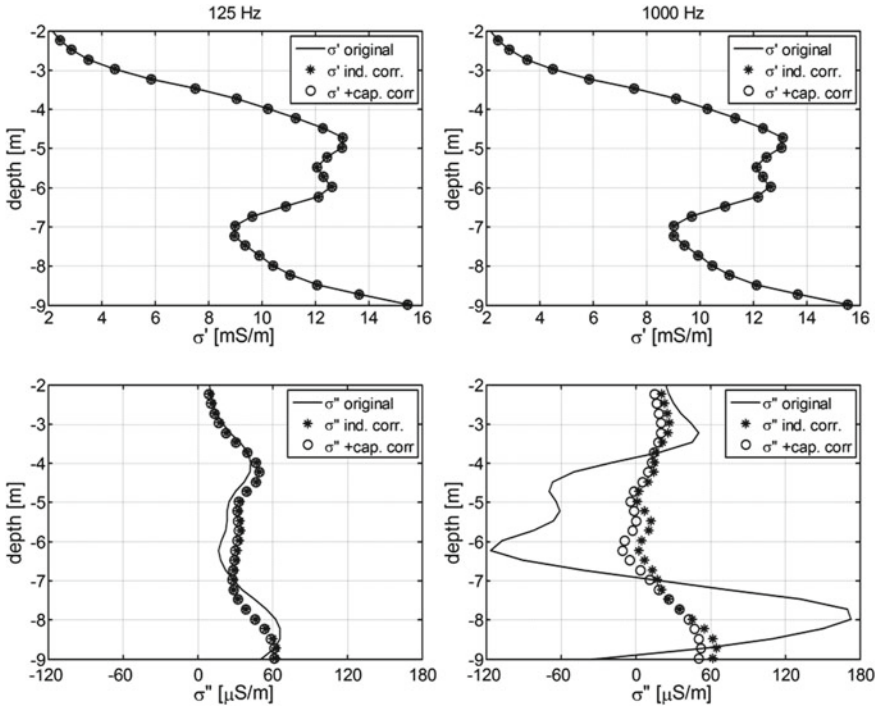


Fig. 1.9 Depth profiles of real (*top*) and imaginary (*bottom*) conductivity at 125 Hz (*left*) and 1 kHz (*right*) as obtained from EIT measurements in borehole 76 at the Krauthausen test site, with (*open symbols*) and without (*solid curves*) corrections for inductive and capacitive coupling, using a 1D inversion scheme

layered subsurface (1D inversion). This inversion involves an axisymmetric 2D forward modeling problem. The corresponding 2D finite-element modeling, however, is a simple extension of 2D finite-element modeling in terms of Cartesian coordinates where the contribution of each element to the finite-element matrix is multiplied by $2 \pi r$, with r being the radial distance of the element's centroid from the symmetry axis (see, e.g., Kwon and Bang 1997). We also considered capacitive coupling in the axisymmetric 2D forward modeling using the approach outlined above. In particular, we considered two kinds of capacitances. The first one is the frequency-dependent capacitance between the cable isolation and the soil. This capacitance was obtained from the dimensions of the electrode chain and was estimated to be as high as 11,000 pF in the low-frequency range. The second type of capacitance is the input capacitance at the electrode amplifier, which was found to be 40 pF (Zhao et al. 2013). We modified the modeling tools presented in detail in Zimmermann (2011) to simulate such axisymmetric modeling domains with additional capacitances.

The results of this 1D inversion approach for the complex conductivity distribution with depth are shown in Fig. 1.9 for EIT measurements made at 125 Hz and 1 kHz in borehole 76. In a first step, raw EIT measurements were inverted. Especially at 1 kHz,

this resulted in relatively strong variations of σ'' with depth that are not in agreement with the reference EIS measurements (cf. Fig. 1.8). Physically implausible negative values of σ'' are also observed at 1 kHz. After correction of the EIT measurements for inductive coupling effects, the inversion was repeated. The inversions of the data corrected for inductive coupling yield much less variation of σ'' with depth, and physically implausible negative values are not present (Fig. 1.9). The effect of the correction for inductive coupling is much stronger at 1 kHz than at 125 Hz. In parts of the profile, the difference between the corrected and uncorrected σ'' values is as large as $100 \mu\text{S m}^{-1}$, corresponding to phase differences up to ~ 12 mrad. Although this difference is much smaller at 125 Hz, the corrections still amount to $10\text{--}20 \mu\text{S m}^{-1}$ ($\sim 1\text{--}2$ mrad) in parts of the profile. In a final step, the corrected EIT data were inverted using the forward model with integrated capacitances. The effect of this correction for capacitive coupling is clearly apparent at 1 kHz, but it is of secondary importance compared with the correction for inductive coupling. Finally, Fig. 1.9 also shows that σ' is not significantly affected by the correction for inductive and capacitive coupling effects.

The 1D inversion results after correction for inductive and capacitive coupling effects (Fig. 1.9) correspond reasonably well with the laboratory EIS measurements (Fig. 1.8). The general pattern of σ'' is consistent between the two frequencies. The approximately three layers with different σ'' values can also be recognized in the 1D inversion result for the corrected data. The additional decrease of σ'' in the top of the aquifer visible in the inverted depth profile is associated with unsaturated soil above the groundwater table that is not reflected in the laboratory EIS measurements on saturated samples. However, it is also apparent that the accuracy of the corrections can still be improved at 1 kHz. For example, σ'' is still slightly negative in the depth range between 5 and 7 m. We attribute this to additional additive impedances in the calibration measurements that have not yet been considered in the pole-pole matrix used to correct for inductive coupling.

Our second inversion approach is based on a two-dimensional, frequency-dependent parameterization of complex electrical conductivity and uses the spatio-spectral regularization outlined above. It thus represents a 3D inverse problem and involves 2.5D forward modeling (3D source in 2D space, see Kemna 2000 for details) for each considered frequency. The inverted data sets comprise EIT measurements in both boreholes. Data errors were quantified following the approaches of Koestel et al. (2008) and Flores Orozco et al. (2012b). Because it is not straightforward to implement the correction approach for capacitive coupling in the 2.5D forward model, due to the inherent Fourier transform with respect to the strike direction of the assumed 2D spatial distribution, this correction has not yet been considered in the inversion. However, the previous analysis (Fig. 1.9) clearly showed that inductive coupling effects are much stronger and thus their correction is more important for accurate cross-borehole EIT imaging.

The EIT complex conductivity imaging results obtained at 2 Hz, where coupling effects are not yet significant and thus inverted images for data with and without inductive corrections are virtually identical, are shown in Fig. 1.10. The images reveal a general layering as in agreement with the corresponding lab data as well as the 1D

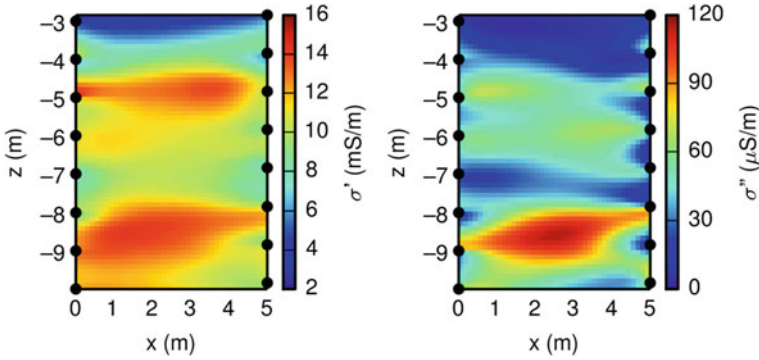


Fig. 1.10 Images of real (*left*) and imaginary (*right*) conductivity at 2 Hz as obtained from EIT measurements in boreholes 75 and 76 at the Krauthausen test site. Black dots indicate position of electrodes in borehole 75 (*left side of the images*) and 76 (*right side of the images*)

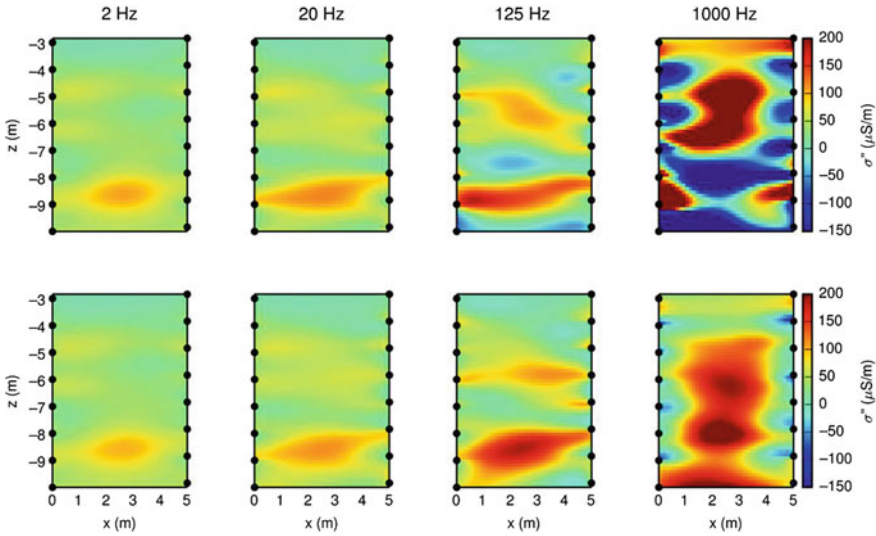


Fig. 1.11 Images of imaginary conductivity at selected frequencies obtained from multi-frequency EIT measurements in boreholes 75 and 76, without (*top panel*) and with (*bottom panel*) corrections for inductive coupling, using the newly developed inversion scheme with spatio-spectral regularization. Black dots indicate position of electrodes (cf. Fig. 1.10)

inversion results (cf. Figs. 1.8 and 1.9). Given the much larger number of measurements taken into account here, a higher vertical resolution is obtained than with the 1D inversion, which is likely to explain the differences with respect to vertical variability and contrast in the recovered values, in particular for the imaginary conductivity σ'' . When inspecting the σ'' images obtained at higher frequencies (Fig. 1.11), the distorting effect of the inductive coupling in the data becomes evident. Inverting the corrected data yields consistent images with a relatively smooth, steady increase of

the imaginary conductivity with frequency in the polarizable sediment layers, as also observed in the laboratory measurements (Fig. 1.8), while without the inductive data correction the images exhibit erratic patterns, with physically meaningless negative values, at frequencies above 100Hz. As already outlined when discussing the 1D inversion results, we expect that there is still room for improving the data correction procedures and thus the achievable image quality, especially for frequencies above 100Hz.

1.5 Conclusions and Outlook

In the 4DEIT project, we have successfully increased the power of spectral EIT technology by developing (i) a new method for spectral regularization in multi-frequency EIT inversion, and (ii) correction procedures for capacitive and inductive coupling in borehole EIT measurements using multi-electrode chains. Spectral regularization was found to provide spectrally smoother changes in the complex electrical conductivity that are more consistent with the typical electrical relaxation behavior of soils, sediments, and rocks. In ideal test conditions, the developed correction methods for inductive and capacitive coupling resulted in an accuracy of 0.8 mrad at 10kHz. Borehole EIT measurements in a heterogeneous aquifer confirmed that EIT measurements above 50Hz were indeed considerably affected by inductive and capacitive coupling effects, as indicated by excessively large and partly physically implausible values for the imaginary part of the electrical conductivity. Application of the newly developed correction procedures showed that inductive coupling effects were considerably stronger than capacitive coupling effects in borehole EIT measurements. After correction, EIT inversion results corresponded reasonably well with the expected range of complex conductivity values derived from laboratory EIS measurements. However, it was also apparent that there is still room to improve the correction methods for inductive coupling, and we are currently in the process of extending the pole-pole matrix used for data correction with additional additive capacitances that have so far not been considered.

We conclude that with the methodological improvements achieved in this project, broadband EIT has become a feasible technology for field-scale surveys, in particular those involving boreholes. In the near future, we hope to transfer the considerable diagnostic potential of broadband electrical spectroscopy with respect to textural, hydraulic, and biogeochemical soil and rock properties to geophysical imaging applications, thus enabling a breakthrough in the spatially highly resolved characterization and diagnosis of subsurface lithology, hydrogeology, and biogeochemistry at depth scales ranging from 1 to 100 m.

Acknowledgments The 4DEIT project was funded by the German Ministry of Education and Research (BMBF) in the framework of the R&D Program GEOTECHNOLOGIEN (Grants 03G0743A, 03G0743B, 03G0743C).

References

- Binley AM, Slater LD, Fukes M, Cassiani G (2005) The relationship between frequency dependent electrical resistivity and hydraulic properties of saturated and unsaturated sandstone. *Water Resour Res* 41:W12417
- Blaschek R, Hördt A, Kemna A (2008) A new sensitivity-controlled focusing regularization scheme for the inversion of induced polarization data based on the minimum gradient support. *Geophysics* 73:F45–F54
- Breede K, Kemna A, Esser O, Zimmermann E, Vereecken H, Huisman JA (2011) Joint measurement setup for determining spectral induced polarization and soil hydraulic properties. *Vadose Zone J* 10:716–726
- Döring U (1997) Transport der reaktiven Stoffe Eosin, Uranin und Lithium in einem heterogenen Grundwasserleiter. Ph.D. thesis, University of Kiel, Germany
- Flores Orozco A, Kemna A, Oberdörster C, Zschornack L, Leven C, Dietrich P, Weiss H (2012a) Delineation of subsurface hydrocarbon contamination at a former hydrogenation plant using spectral induced polarization imaging. *J Cont Hydrol* 136(137):131–144
- Flores Orozco A, Kemna A, Zimmermann E (2012b) Data error quantification in spectral induced polarization imaging. *Geophysics* 77:E227–E237
- Flores Orozco A, Williams KH, Kemna A (2013) Time-lapse spectral induced polarization imaging of stimulated uranium bioremediation. *Near Surf Geophys* 11:531–544
- Kemna A (2000) Tomographic inversion of complex resistivity—theory and application. Ph.D. thesis, Ruhr-University of Bochum, Germany
- Kemna A, Binley A, Ramirez A, Daily W (2000) Complex resistivity tomography for environmental applications. *Chem Eng J* 77:11–18
- Kemna A, Vanderborght J, Kulesa B, Vereecken H (2002) Imaging and characterisation of subsurface solute transport using electrical resistivity tomography (ERT) and equivalent transport models. *J Hydrol* 267:125–146
- Kemna A, Binley A, Slater L (2004) Crosshole IP imaging for engineering and environmental applications. *Geophysics* 69:97–107
- Kemna A, Binley A, Cassiani G, Niederleithinger E, Revil A, Slater L, Williams KH, Haegel F-H, Hördt A, Kruschwitz S, Leroux V, Titov K, Zimmermann E (2012) An overview of the spectral induced polarization method for near-surface applications. *Near Surf Geophys* 10:453–468
- Koestel J, Kemna A, Javaux M, Binley A, Vereecken H (2008) Quantitative imaging of solute transport in an unsaturated and undisturbed soil monolith with 3-D ERT and TDR. *Water Resour Res* 44:W12411
- Kwon YW, Bang H (1997) The finite element method using MATLAB. Florida, Boca Raton
- Leroy P, Revil A, Kemna A, Cosenza P, Ghorbani A (2008) Complex conductivity of water-saturated packs of glass beads. *J Colloid Interface Sci* 321(1):103–117
- Madden TR, Cantwell T (1967) Induced polarization, a review. In: Hansen DA, Heinrichs WE Jr. Holmer RC, MacDougall RE, Rogers GR, Sumner JS, Ward SH (eds) *Society of exploration geophysicists' mining geophysics, vol II*. pp 373–400
- Müller K, Vanderborght J, Englert A, Kemna A, Rings J, Huisman JA, Vereecken H (2010) Imaging and characterization of solute transport during two tracer tests in a shallow aquifer using electrical resistivity tomography and multilevel groundwater samplers. *Water Resour Res* 46:W03502
- Revil A, Florsch N (2010) Determination of permeability from spectral induced polarization in granular media. *Geophys J Int* 181:1480–1498
- Revil A (2013) On charge accumulations in heterogeneous porous materials under the influence of an electrical field. *Geophysics* 78(4):D271–D291
- Slater LD, Lesmes D (2002) IP interpretation in environmental investigations. *Geophysics* 67:77–88
- Sunde ED (1968) *Earth conduction effects in transmission systems*. Dover Publications, New York
- Tillmann A, Englert A, Nyari Z, Fejes I, Vanderborght J, Vereecken H (2008) Characterization of subsoil heterogeneity, estimation of grain size distribution and hydraulic conductivity at the Krauthausen test site using cone penetration test. *J Contam Hydrol* 95:57–75

- Vanderborght J, Kemna A, Hardelauf H, Vereecken H (2005) Potential of electrical resistivity tomography to infer aquifer transport characteristics from tracer studies: a synthetic case study. *Water Resour Res* 41:W06013
- Vanhala H (1997) Mapping oil-contaminated sand and till with the spectral induced polarization (SIP) method. *Geophys Prospect* 45:303–326
- Vereecken H, Döring U, Hardelauf H, Jaekel U, Hashagen U, Neuendorf O, Schwarze H, Seidemann R (2000) Analysis of solute transport in a heterogeneous aquifer: the Krauthausen field experiment. *J Contam Hydrol* 45(3–4):329–358
- Williams KH, Kemna A, Wilkins MJ, Druhan J, Arntzen E, N’Guessan AL, Long PE, Hubbard SS, Banfield JF (2009) Geophysical monitoring of coupled microbial and geochemical processes during stimulated subsurface bioremediation. *Environ Sci Technol* 43:6717–6723
- Zhao Y, Zimmermann E, Huisman JA, Treichel A, Wolters B, van Waasen S, Kemna A (2013) Broadband EIT borehole measurements with high phase accuracy using numerical corrections of electromagnetic coupling effects. *Meas Sci Tech* 24(8):085005
- Zimmermann E, Kemna A, Berwix J, Glaas W, Munch HM, Huisman JA (2008a) A high-accuracy impedance spectrometer for measuring sediments with low polarizability. *Meas Sci Tech* 19:105603
- Zimmermann E, Kemna A, Berwix J, Glaas W, Vereecken H (2008b) EIT measurement system with high phase accuracy for the imaging of spectral induced polarization properties of soils and sediments. *Meas Sci Tech* 19:094010
- Zimmermann E, Huisman JA, Kemna A, Berwix J, Glaas W, Meier H, Wolters B, Esser O (2010) Advanced electrical impedance tomography system with high phase accuracy. In: *Proceedings of the 6th World Congress on industrial process tomography (WCIPT6)*, Beijing, China, pp 583–591, 6–9 Sept 2010
- Zimmermann E (2011) *Phasengenaue Impedanzspektroskopie und -tomographie für geophysikalische Anwendungen*. Ph.D. thesis, University of Bonn, Germany